

Very High Interfacial Thermal Conductance in Fully hBN-Encapsulated MoS₂ van der Waals Heterostructure

Fan Ye¹, Qingchang Liu², Baoxing Xu^{2*}, Philip X.-L. Feng^{1,3*}, Xian Zhang^{4*}

¹*Department of Electrical Engineering & Computer Science, Case School of Engineering,
Case Western Reserve University, Cleveland, OH 44106, USA*

²*Department of Mechanical and Aerospace Engineering,
University of Virginia, Charlottesville, VA 22904 USA*

³*Department of Electrical & Computer Engineering, Herbert Wertheim College of Engineering,
University of Florida, Gainesville, FL 32611, USA*

⁴*Department of Mechanical Engineering,
Stevens Institute of Technology, Hoboken, NJ 07030 USA*

Abstract

We report experimental and computational studies of thermal transport properties in hexagonal boron nitride (hBN) encapsulated molybdenum disulfide (MoS₂) structure using refined optothermal Raman techniques, and reveal very high interfacial thermal conductance between hBN and MoS₂. By studying the Raman shift of hBN and MoS₂ in suspended and substrate-supported thin films under varying laser power and temperature, we calibrate lateral (in-plane) thermal conductivity of hBN and MoS₂ and the vertical interfacial thermal conductance in the hBN/MoS₂/hBN heterostructure as well as the interfaces between heterostructure and substrate. Crucially, we have found that interfacial thermal conductance between hBN and encapsulated MoS₂ is 74 ± 25 MW/m²K and 72 ± 22 MW/m²K in supported and suspended films, respectively, which are significantly higher than interfacial thermal conductance between MoS₂ and other substrates. Molecular dynamics (MD) computations conducted in parallel have shown consistent results. This work provides clear evidence of significantly efficient heat dissipation in hBN/MoS₂/hBN heterostructures and sheds light on building novel hBN encapsulated nanoelectronics with efficient thermal management.

Introduction

Atomically thin crystalline materials [1,2,3,4,5,6,7] have spurred increasing research interests owing to their attractive electronic [1,2,3,7,8], optical [4,7,9,10,11], mechanical [12], and energy harvesting [13,14] properties for enabling novel two-dimensional (2D) devices that hold promises for future information technologies [13,15,16,17]. The advances in mechanical assembly techniques [3,8,18] and synthesis methods [19] empower researchers to construct van der Waals heterostructures by creating and stacking various 2D layers together. Among several van der Waals heterostructure platforms, hexagonal boron nitride (hBN) encapsulated structures, sandwiching one or several 2D layers within two hBN layers (*e.g.*, hBN/MoS₂/hBN), have been demonstrated with significant improvements in device performance [3,8,18,20,21,22]. In comparison with the mainstream Si or SiO₂ substrate, hBN, thanks to its strong in-plane ionic bonding of the planar hexagonal lattice structure, offers a flatter surface which screens the dangling bonds and Coulomb scattering effectively [3]. In electronic domain, fully hBN encapsulated MoS₂ field-effect transistors (FETs) with graphite electrodes exhibit Hall mobility up to 34,000 cm²/Vs, which is ten-fold enhancement compared with MoS₂ FETs on bare SiO₂ [8]. A similar electron mobility boost is also observed in hBN encapsulated graphene FETs [18]. In photonic domain, hBN encapsulated graphene devices have been demonstrated as a high-speed electro-optic modulator with a modulation depth of 3.2 dB and a cutoff frequency of 1.2 GHz [21]. Moreover, thanks to hBN's excellent thermal transport properties [23,24,25,26,27,28], electrical insulation, and chemical inertness, hBN encapsulated devices exhibit excellent stability in harsh environments (*e.g.*, high humidity and elevated temperature up to 200°C) over a long term [22].

Though superior electronic performance has been demonstrated in hBN encapsulated structures, thermal properties, including both lateral (in-plane) and interfacial (out-of-plane)

thermal transport in hBN encapsulated structures, remain unexplored. Moreover, in the present effort on achieving high-performance 2D devices, low interfacial thermal conductance between 2D materials and substrates, resulting in inefficient heat dissipation, is regarded as one of the main limitations [29]. For example, the interfacial thermal conductance between MoS₂ and SiO₂ is in the range of 0.4 - 14 MW/m²K [29,30] and thus the heat dissipation in MoS₂ FETs on SiO₂ is quite inefficient, which plagues the performance of MoS₂ FETs. Besides, in MoS₂/hBN heterostructures with hBN only on one side, the interfacial thermal conductance between MoS₂ and hBN is around 17.0 ± 0.4 MW/m²K [28], indicating simply stacking MoS₂ on top of hBN may not facilitate heat dissipation sufficiently. Therefore, considering the excellent promises of hBN encapsulated 2D devices and inefficient heat dissipation of 2D materials in various device structures, a comprehensive study on thermal transport of hBN encapsulated structure is of great importance.

In this work, lateral and interfacial thermal transport properties in fully hBN encapsulated single-layer MoS₂ sandwich structure (hBN/MoS₂/hBN) are carefully studied using the refined optothermal Raman technique [30]. We have found the lateral thermal conductivity of top hBN, bottom hBN, and middle MoS₂ are 428 ± 81 W/mK, 450 ± 83 W/mK, and 83 ± 33 W/mK, which are similar to values in previous studies [26,30,31]. In opto-thermal Raman technique, Raman laser is able to transmit through and is absorbed by each 2D layer to provide heat source and to obtain temperature information from the reflected Raman signals by each 2D layer. As the laser power is increased, sample is heated, which enables red-shift Raman mode due to thermal softening. Thermal modeling can then be used to extract the thermal conductivity and interfacial thermal conductance from the measured shift rate. Interestingly, the interfacial thermal conductance in the hBN/MoS₂/hBN sandwich structure is about 72 ± 22 MW/m²K, which is significantly higher than the thermal conductance between MoS₂ and other substrates

[28,30,32,33,34], suggesting the fully hBN encapsulation platform offers a much efficient heat dissipation than in other structures. Molecular dynamics (MD) calculations of the interfacial thermal conductance in hBN encapsulated structure agree well with the experimental results and provide the theoretical proof. This work not only demonstrates that the hBN fully encapsulated structures provide much efficient heat dissipation for the encapsulated layers, but also sheds light on engineering new-generation nanoelectronics.

Results and Discussions

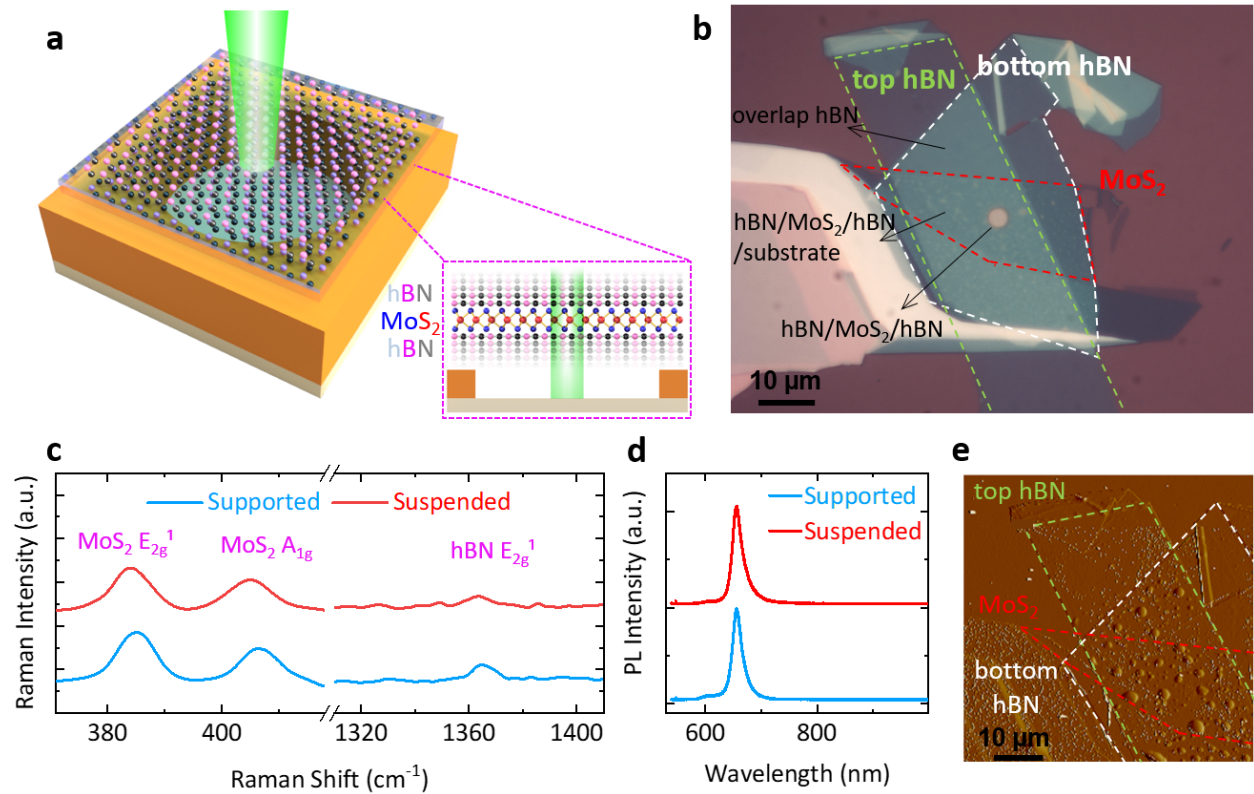


Figure 1. hBN/MoS₂/hBN sample configuration and characterization. (a) Illustration of a circular drumhead hBN/MoS₂/hBN van der Waals heterostructure suspended device and Raman measurement scheme. *Inset*: side view illustration of an hBN/MoS₂/hBN device and measurement scheme. (b) An optical microscopy image of an hBN/MoS₂/hBN van der Waals heterostructure with top hBN, bottom hBN, overlap hBN, supported hBN/MoS₂/hBN/substrate and suspended hBN/MoS₂/hBN. (c) Raman, (d) photoluminescence (PL), and (e) atomic force microscopy (AFM) of the hBN/MoS₂/hBN van der Waals heterostructure device.

The device structure and measurement scheme are illustrated in Fig. 1a. An hBN/MoS₂/hBN van der Waals heterostructure sitting on top of a pre-patterned substrate is heated by a 514 nm laser photothermally. Besides heating up the device, the 514 nm laser is also used to measure the Raman shift which indicates the device temperature and thus calibrate the thermal transport properties. The fabrication of hBN encapsulated MoS₂ devices starts from exfoliating hBN and single-layer MoS₂ on PDMS to ensure the pristine physical properties. After obtaining the samples on PDMS, bottom hBN, MoS₂, and top hBN are stacked one by one on pre-patterned substrates with circular microtrenches (diameter 3 μm and depth 290 nm) using the van der Waals transfer method [35]. A microscope image of an hBN/MoS₂/hBN device with 3 μm diameter hole is shown in Fig. 1b. After the device fabrication, Raman (Fig. 1c) and photoluminescence (PL) (Fig. 1d) measurements are conducted to characterize the device. From the Raman spectroscopy, two MoS₂ characteristic peaks and one hBN characteristic peak are observed in both suspended and supported regions, which confirms the quality of hBN/MoS₂/hBN heterostructure in both regions. As there is a clear direct bandgap peak but no indirect bandgap peak in PL, it is confirmed that the MoS₂ is one-atomic-layer. Based on atomic force microscopy (AFM) measurements (Fig. 1e), the thicknesses of top hBN and bottom hBN are 10.6 nm and 16.8 nm respectively.

The temperature dependent Raman shift for both MoS₂ and hBN was investigated. By gradually increasing the substrate's temperature from 295 K to 495 K, Raman shift of MoS₂ and hBN in both supported regions and suspended regions are measured. Fig. 2a presents the schematic of the optothermal Raman technique to measure the lateral thermal conductivity and interfacial thermal conductance. Raman laser is transmitting through each layer of the heterostructure and the reflected spectra include temperature information of each layer. Fig. 2b, c presents an example of the temperature-dependent Raman spectra of supported MoS₂ and hBN.

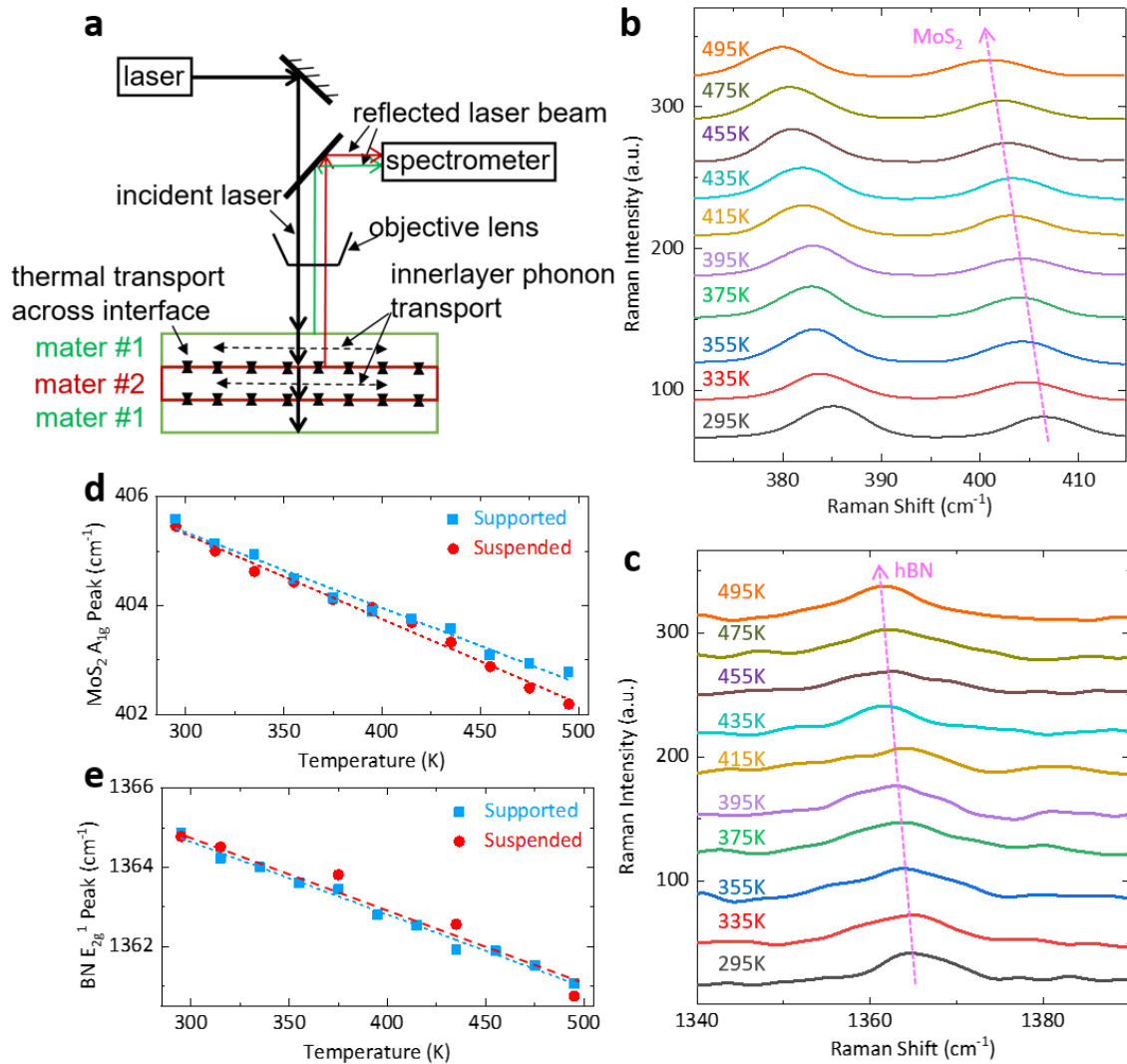


Figure 2. Schematic of optothermal Raman technique and temperature dependent Raman shifts of hBN/MoS₂/hBN heterostructure. (a) Schematic of the optothermal Raman technique. Raman spectroscopy curves of (b) MoS₂ and (c) hBN as temperature increases from 295 K to 495 K. The evolution and fitting of (d) MoS₂ A_{1g} and (e) hBN E_{2g}⁻¹ Raman peak position.

The Raman peaks of MoS₂ and hBN in both supported and suspended regions show red shift as temperature rises due to the thermally driven bond softening, as previously observed for graphene, MoS₂ and MoSe₂ [30, 36]. By fitting Raman peaks, the temperature dependence of MoS₂ A_{1g} peak shift and hBN E_{2g}⁻¹ peak shift is shown in Fig. 2d and Fig. 2e respectively. It is observed that MoS₂ A_{1g} peak in suspended region exhibits higher temperature dependence than the supported region,

which is attributed to the interaction between MoS₂ and substrate as MoS₂ A_{1g} peak is out-of-plane vibration mode. In contrast, Raman peak of hBN in suspended region and supported region show similar temperature dependence. By fitting the temperature dependent Raman peak position (Fig. 2c, d) using linear functions, the first-order temperature coefficients (slopes) for hBN and MoS₂ in suspended and supported are determined (Table 1).

After obtaining the first-order temperature coefficients for MoS₂ and hBN, thermal transport properties of hBN/MoS₂/hBN are investigated through photothermal heating the van der Waals heterostructure in both suspended and supported regions. The power adsorbance of hBN and MoS₂ to 514 nm laser is calculated and summarized in Table 1. Fig. 3a-d show the Raman shift versus the absorbed laser power of supported MoS₂, suspended MoS₂, and supported and suspended hBN

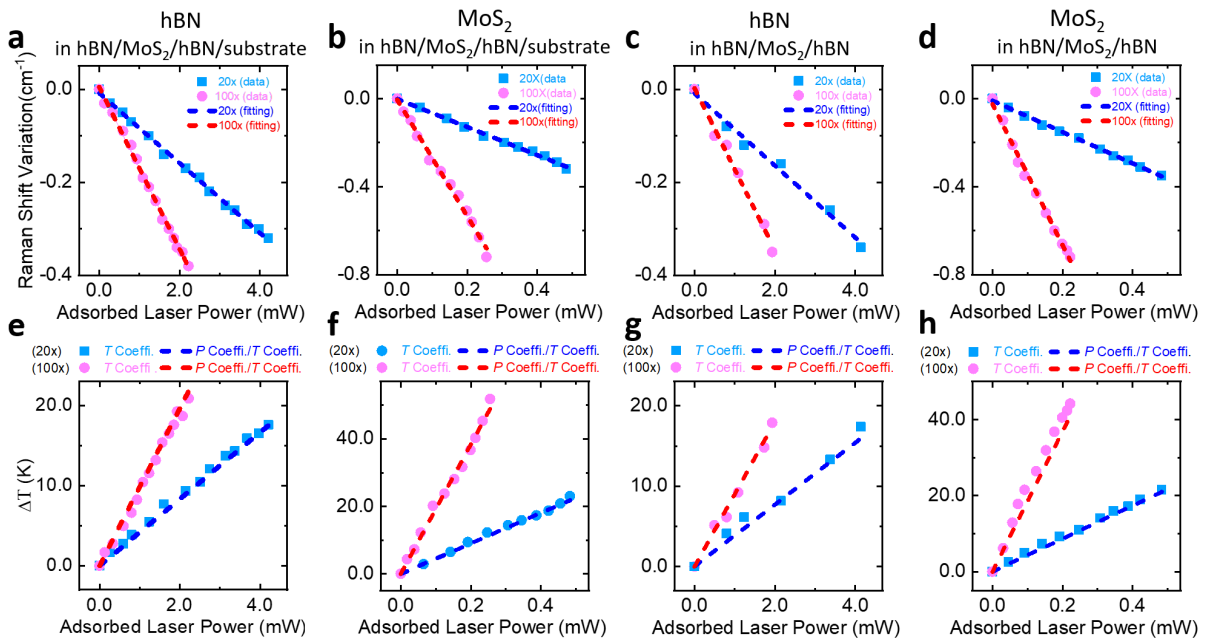


Figure 3. Power dependent Raman peak shift measured using different laser spot sizes of (a) hBN in supported hBN/MoS₂/hBN structure, (b) MoS₂ in supported hBN/MoS₂/hBN structure, (c) hBN in suspended hBN/MoS₂/hBN structure, and (d) MoS₂ in suspended hBN/MoS₂/hBN structure, and temperature variation of these four samples (e), (f), (g), (h) induced by photothermal heating corresponding to (a), (b), (c), and (d) respectively.

Table 1: First-order temperature coefficients, absorbance, and power coefficients of hBN and MoS₂ in different structures.

Interface	Sample location	Temperature coefficient (cm ⁻¹ /K)	Thickness (nm)	Absorbance (%)	Power coefficient (cm ⁻¹ /μW)	
					0.19 μm spot	0.41 μm spot
hBN/MoS ₂ /hBN	Supported	MoS ₂ : -0.0139 ± 0.0024	0.65	3.8 ± 0.1	-0.1021 ± 0.0081	-0.0241 ± 0.0017
		hBN: -0.0183 ± 0.0023	27.4	33.4 ± 0.2	-0.0600 ± 0.0060	-0.0254 ± 0.0023
	Suspended	MoS ₂ : -0.0163 ± 0.0028	0.65	3.8 ± 0.1	-0.1150 ± 0.0123	-0.0271 ± 0.0030
		hBN: -0.0196 ± 0.0022	27.4	33.4 ± 0.2	-0.0588 ± 0.0047	-0.0251 ± 0.0018
hBN/SiO ₂	Top hBN only	hBN: -0.0229 ± 0.0023	10.6	16.7 ± 0.2	-0.0857 ± 0.0141	-0.0338 ± 0.0159
	Bottom hBN only	hBN: -0.0178 ± 0.0030	16.8	25.0 ± 0.2	-0.0739 ± 0.0179	-0.0325 ± 0.0110
	Overlap hBN only	hBN: -0.0232 ± 0.0023	27.4	37.2 ± 0.2	-0.1179 ± 0.0273	-0.0325 ± 0.0171

with top and bottom layers measured simultaneously. By gradually increasing the laser power, Raman peaks of both MoS₂ and hBN show red shift as laser power increases, indicating the temperature increase of each layer of the van der Waals heterostructure. For MoS₂ and hBN in both suspended and supported regions, Raman peak position exhibits a larger red shift from the 100× objective (spot size 0.19 μm) than the 20× objective (spot size 0.41 μm), which is attributed to the higher power absorbed when a larger spot size is applied. Based on the extracted power dependent Raman peak positions, first-order power coefficient is calculated and summarized in Table 1.

For each objective, the spot size was obtained by scanning across a sharp flake edge, and fitting the measured Raman peak intensity corresponding to the position using a Gaussian error function. The obtained spot size of 100× objective is 0.19 μm, and that of the 20× objective is 0.41 μm.

To determine the absolute power absorbed for heat flow analysis, hBN membranes were separately exfoliated onto transparent quartz substrates, and their measured absorption spectra were used to determine the frequency-dependent complex dielectric function. The dielectric functions of sample, along with that of the substrate material, were then used to calculate the absorption coefficient at 514 nm using the standard transfer matrix method. The absorption

coefficient α of hBN can be determined by the measured optical transmittance T_e from the following equation [37]:

$$T_e = \frac{(1-R)^2 \exp(-\alpha d)}{1-R^2 \exp(-2\alpha d)} \quad (1)$$

where d is the sample thickness, and in the case of normal incidence, R can be expressed simply as a function of the refractive index n , $R = (n-1/n+1)^2$, with $n = 1.62$ at 514 nm wavelength. The obtained α is 3730 cm^{-1} . Including the thickness d , the value of optical absorbance of top hBN, bottom hBN, and overlap hBN are $16.7 \pm 0.2 \%$, $25.0 \pm 0.2 \%$, and $37.2 \pm 0.2\%$, and that of one-atomic-layer MoS₂ is $5.2 \pm 0.1 \%$ at 514 nm wavelength. For the hBN/MoS₂/hBN heterostructure, the transmittance of top hBN is 74.2 % and that of MoS₂ is 89.87 %, so the absolute absorbance of MoS₂ in the hBN/MoS₂/hBN heterostructure is $3.8 \pm 0.1 \%$, and that of the top and bottom hBN considered together is $33.4 \pm 0.2 \%$ (Table 1). Due to the low quantum yield of as-exfoliated MoS₂ and hBN, the absorbed energy emitting as photons is ignored.

The estimated temperature variation induced by photothermal heating and power absorbed by each 2D layer allow us to calculate the thermal conductivity and interfacial thermal conductance in the hBN/MoS₂/hBN van der Waals heterostructure. Based on the Gaussian profile of laser and spot radius of r_0 , the volumetric heating power density $q'''(r)$ of each layer in the heterostructure is presented as:

$$q'''(r) = P \cdot \frac{1}{t} \cdot \frac{1}{\pi r_0^2} \exp\left(-\frac{r^2}{r_0^2}\right) \quad (2)$$

where P is absorbed laser power, t is sample thickness, r is the distance to laser spot center which varies from 0 to ∞ . Considering the interfacial thermal conductance between MoS₂ and hBN that's

encapsulating it, the temperature distribution $T(r)$ in the target layer (MoS₂) of the van der Waals heterostructure is represented using a cylindrical coordinate as:

$$\frac{1}{r} \frac{d}{dr} \left(r \frac{dT(r)}{dr} \right) - \frac{g}{\kappa t} (T(r) - T_a(r)) + \frac{q'''(r)}{\kappa} = 0 \quad (3)$$

where κ is thermal conductivity, g is interfacial thermal conductance at the interface between the two material layers with temperatures $T(r)$ and $T_a(r)$ respectively. The boundary conditions of the photothermal heating are described as $\frac{dT}{dr} \Big|_{r=0} = 0$ and $T(r \rightarrow \infty) = 298 \text{ K}$. The measured temperature T_m using Raman shift is the weighted average of the local temperature distribution $T(r)$:

$$T_m = \frac{\int_0^\infty T(r) \exp\left(-\frac{r^2}{r_0^2}\right) r dr}{\int_0^\infty \exp\left(-\frac{r^2}{r_0^2}\right) r dr} \quad (4)$$

The measured temperature T_m and absorbed laser power P of each layer has a relation of thermal resistance R_m (K/W) as a ratio between them, which is obtained by dividing power dependent Raman shift (cm⁻¹/W) over temperature dependent Raman shift (cm⁻¹/K). The temperature variations of MoS₂ and hBN as a relation to the absorbed laser power are shown in Fig. 3e-h.

To extract thermal transport properties including lateral thermal conductivity κ and interfacial thermal conductance g , we apply the same mathematic methods in ref. 30 and ref. 38. In brief, by solving Equations 2–4, we are able to determine a thermal resistance R_m that is a function of intralayer thermal conductivity κ and interfacial thermal conductance g . Since both MoS₂ and hBN have temperature increase with laser heating, the ratio between the temperature

increase of them is used for obtaining the interfacial thermal conductance g between MoS₂ and the hBN membranes encapsulating it. Using the first-order power coefficient (cm^{-1}/W) and temperature coefficient (cm^{-1}/K) R_m (K/W) with $0.19 \mu\text{m}$ spot size ($100\times$) and $0.41 \mu\text{m}$ ($20\times$), the lateral thermal conductivity κ and interfacial thermal conductance g are calculated and summarized in Table 2. We obtained the lateral thermal conductivities of MoS₂ in the hBN/MoS₂/hBN encapsulated structure in both supported and suspended regions, bottom hBN alone, top hBN alone, and the overlap hBN of bottom and top hBN samples. The lateral thermal conductivities are $83 \pm 33 \text{ W/mK}$ (for MoS₂), $450 \pm 83 \text{ W/mK}$ (for bottom hBN), $428 \pm 81 \text{ W/mK}$ (for top hBN), and $420 \pm 74 \text{ W/mK}$ (for overlap hBN). The interfacial thermal conductance is $74 \pm 25 \text{ MW/m}^2\text{K}$ (between MoS₂ and hBN in the encapsulated structure), $69 \pm 23 \text{ MW/m}^2\text{K}$ (between top hBN and substrate), $72 \pm 22 \text{ MW/m}^2\text{K}$ (between bottom hBN and substrate), and $66 \pm 21 \text{ MW/m}^2\text{K}$ (between overlap hBN and substrate). Based on the calculation, the thermal conductance of the hBN/SiO₂ interface is similar to the previously reported values [39]. In contrast, hBN/MoS₂/hBN interface in the encapsulated structure exhibits a much higher interfacial thermal conductance than that in MoS₂/SiO₂ interface [29,30], suggesting the hBN encapsulation platform provides much efficient heat dissipation for MoS₂. The thermal conductivity and interfacial thermal conductance in suspended region are calculated iteratively with thermal transport parameters obtained from the measurements using Eq. 2-4. The lateral thermal conductivity of MoS₂ in encapsulated structure in suspended region is 85 W/mK and the interfacial thermal conductance of the hBN/MoS₂/hBN interface is $72 \pm 22 \text{ MW/m}^2\text{K}$, which are similar to the values in supported region on the same sample. Here the lateral thermal conductivity of single-layer MoS₂ in the hBN encapsulated structure is comparable to that of the suspended MoS₂, which is significantly higher than the supported MoS₂ on the amorphous substrate (SiO₂, Au, etc.) [29,30].

This is explained by the relatively small lattice mismatch and the ultra-clean surface in the van der Waals interface between MoS₂ and hBN [40].

Table 2: Lateral thermal conductivities and interfacial thermal conductance in hBN/MoS₂/hBN van der Waals heterostructure device, and the hBN on substrate alone.

Interface	Sample location	Thermal conductivity (W/mK)	Interfacial thermal conductance (MW/m ² K)
hBN/MoS ₂ /hBN	Supported	MoS ₂ : 83 ± 33	74 ± 25
	Suspended	MoS ₂ : 85 ± 36	72 ± 22
hBN/SiO ₂	Top hBN only	hBN: 428 ± 81	69 ± 23
	Bottom hBN only	hBN: 450 ± 83	72 ± 26
	Overlap hBN only	hBN: 420 ± 74	66 ± 21

To gain further insights into the heat transport in hBN encapsulated MoS₂ structure, molecular dynamics (MD) calculation is performed. The device configuration for MD simulation is shown in Fig. 4a. One-atomic-layer MoS₂ sandwiched by two hBN membranes is supported on substrate and a supported fully hBN-encapsulated MoS₂ (hBN/MoS₂/hBN/substrate) structure is therefore constructed. Similar procedures are applied to build the suspended hBN/MoS₂/hBN, hBN/MoS₂, and hBN/MoS₂/Si structures. The intralayer bonded interaction in hBN and MoS₂ is described by the many-body tersoff [41] and Stillinger-weber potential [42], respectively, while the substrate is described by the edip potential. The non-bonded interlayer interaction among hBN, MoS₂ and substrate are described by the 12-6 Lennard-Jones (L-J) potential, $E_{vdW} = 4\epsilon[(\sigma/r)^{12} - (\sigma/r)^6]$, where ϵ is the potential well depth, r is the distance between different atoms, and σ is the parameter associated with the equilibrium distance [43]. The periodic boundary conditions are applied in the x and y directions to eliminate the size effect and free boundary condition was applied in the z-direction to exclude the influence of upper and bottom boundaries. The transient heating technique is employed in the simulations, which has been widely used in the exploration of interfacial thermal conductance of 2D heterostructures in both experiments [28,44] and simulations [43,45]. This method is conducted as follows (Fig. 4b). The system is firstly

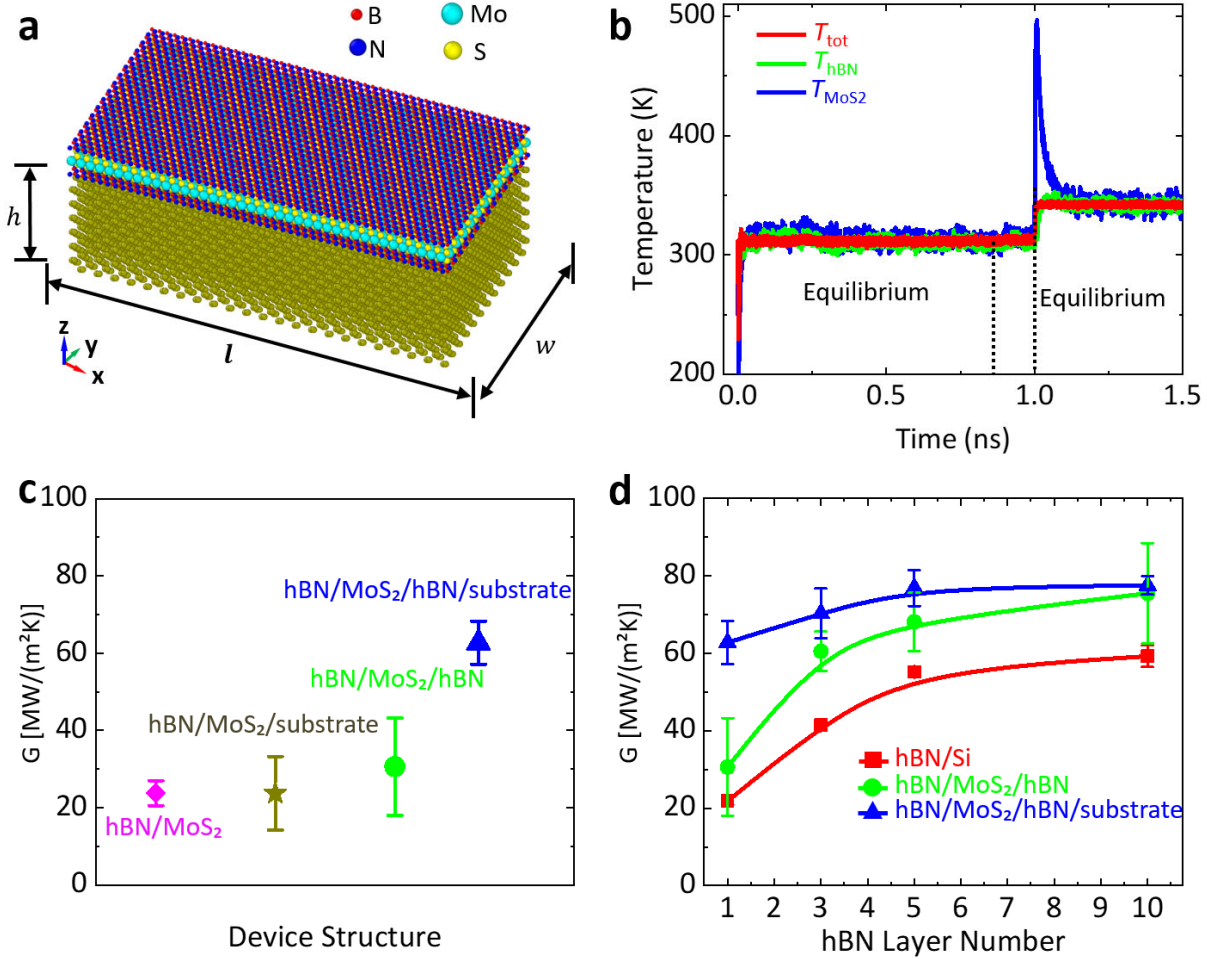


Figure 4. Molecular dynamics (MD) calculation of interfacial transport properties in MoS₂/hBN interfaces. (a) Illustration of molecular dynamic calculation in the supported hBN/MoS₂/hBN/substrate. (b) Temperature evolution of MoS₂ (heat source, T_{MoS_2}), hBN (buffer layers, T_{hBN}) and the system (T_{tot}) after the laser excitation. (c) Comparison of the interfacial thermal conductance between different structures: suspended hBN/MoS₂, supported hBN/MoS₂/substrate, suspended hBN/MoS₂/hBN, and supported hBN/MoS₂/hBN/substrate. (d) Variation of interfacial thermal conductance with layer number of hBN for different device structures.

equilibrated under NVT ensemble with a nose-hoover thermostat for 1 ns to make sure the system has reached its initial equilibrium temperature. After that, the NVE ensemble is employed and the MoS₂ membrane is exposed to an ultrafast heat impulse, which increases the temperature of MoS₂ membrane dramatically in a short time (~ 10 ps). Since the MoS₂ is sandwiched by hBN membranes on both sides, the only path to dissipate thermal energy is from the MoS₂ to hBN. As a result, the

temperature of MoS₂ (T_{MoS_2}) decreases while the temperature of hBN (T_{hBN}) increases in the subsequent relaxation process. As the relaxation process continues, the temperature difference between MoS₂ and hBN decreases and the system reaches a new equilibrium state after a sufficiently long time (~200 ps). The thermal conductance at this final equilibrium temperature is described as follows. The total energy of MoS₂ (E_{tot}) is impacted by thermal dissipation. The evolution of energy of E_t is related to the temperature difference between MoS₂ and hBN ($T_{\text{MoS}_2} - T_{\text{hBN}}$). The interfacial thermal conductance g can be calculated via $\frac{\partial E}{\partial t} = AG(T_{\text{MoS}_2} - T_{\text{hBN}})$, where A is the interfacial area and t is time.

Fig. 4c shows the interfacial thermal conductance between hBN and MoS₂ for different structures of the system at $T_{\text{tot}} = 341$ K. For suspended hBN/MoS₂ structure, the estimated thermal conductance is $g = 23.8$ MW/m²K, which is very close to that in supported area $g = 23.7$ MW/m²K. In contrast, the interfacial thermal conductance in suspended hBN/MoS₂ is $g = 30.6$ MW/m²K, indicating that the encapsulated structure promotes the heat dissipation for MoS₂. The hBN encapsulated MoS₂ heterostructure in supported area – hBN/MoS₂/hBN/substrate exhibits interfacial thermal conductance $g = 62.7$ MW/m²K, which is 160% higher than that in hBN/MoS₂/substrate structure and higher than that in suspended hBN/MoS₂/hBN. The extra high conductance is ascribed to the synergistic effect of the substrate and the encapsulated structure, where bottom hBN serves as a bridging layer to transport the thermal energy from MoS₂ to silicon. However, our experimental results indicate that hBN encapsulated MoS₂ in suspended area (hBN/MoS₂/hBN/substrate) and supported area (hBN/MoS₂/hBN) exhibit very close thermal conductance values (74 MW/m²K and 72 MW/m²K respectively). Considering there are multiple layers (30~50) of hBN in the experiments, it is reasonable to assume thicker hBN exhibits a higher thermal capacity, and as a result, the thermal conductance between hBN and MoS₂ become close

between the suspended and supported structures. To validate this assumption, a series of simulations with different numbers of hBN layers is performed to probe the interfacial thermal conductance between hBN and MoS₂. Fig. 4d presents the variation of thermal conductance with the layer number of hBN in different device structure at $T_{\text{tot}} = 341\text{K}$. For the suspended hBN encapsulated MoS₂ (hBN/MoS₂/hBN) structure, interfacial thermal conductance increases with layer number significantly and reaches 75.5 MW/m²K when the layer number of bottom and top hBN approaches ten. For supported hBN encapsulated MoS₂ structure (hBN/MoS₂/hBN/substrate), interfacial thermal conductance also increases with hBN layer number enhances, though with a much slower rate compared with suspended structure, and reaches 77.5 MW/m²K when hBN layer number approaches 10. The calculated interfacial thermal conductance is close to experimental results in both suspended structures and supported areas, which validates our experimental results. It is worth noting interfacial thermal conductance between suspended and supported structures become increasingly close with hBN becoming thicker, demonstrating the previous assumption that thicker hBN layer membranes provide rise to a higher thermal capacity.

Finally, we benchmark the results by comparing the interfacial thermal conductance in hBN encapsulated structure and other structures within a temperature range between 295K to 450K [28,30,32,33,34] (Fig. 5). Apparently, the interfacial thermal conductance in hBN/MoS₂/hBN van der Waals heterostructure in the vertical direction is significantly higher than MoS₂ with other materials. This ultra-high interfacial thermal conductance is mainly attributed to the relatively small lattice mismatch between hBN and MoS₂ [46], the high thermal conductivity of hBN, and the excellent encapsulation and contact condition in the hBN/MoS₂/hBN van der Waals heterostructure. It is also worth noting that the interfacial thermal conductance in hBN encapsulated MoS₂ is higher than the MoS₂ on hBN non-encapsulated structure [28]. This could

be explained by the fact that the encapsulated structure allows MoS₂ to dissipate heat through both top surface and bottom surface, while in the MoS₂ on hBN structure, the heat in MoS₂ could only dissipate to hBN through the bottom surface. Moreover, the top and down hBN provides a compact and excellent contact conditions in the hBN/MoS₂/hBN sandwich structure which ensures a high interfacial thermal conductance.

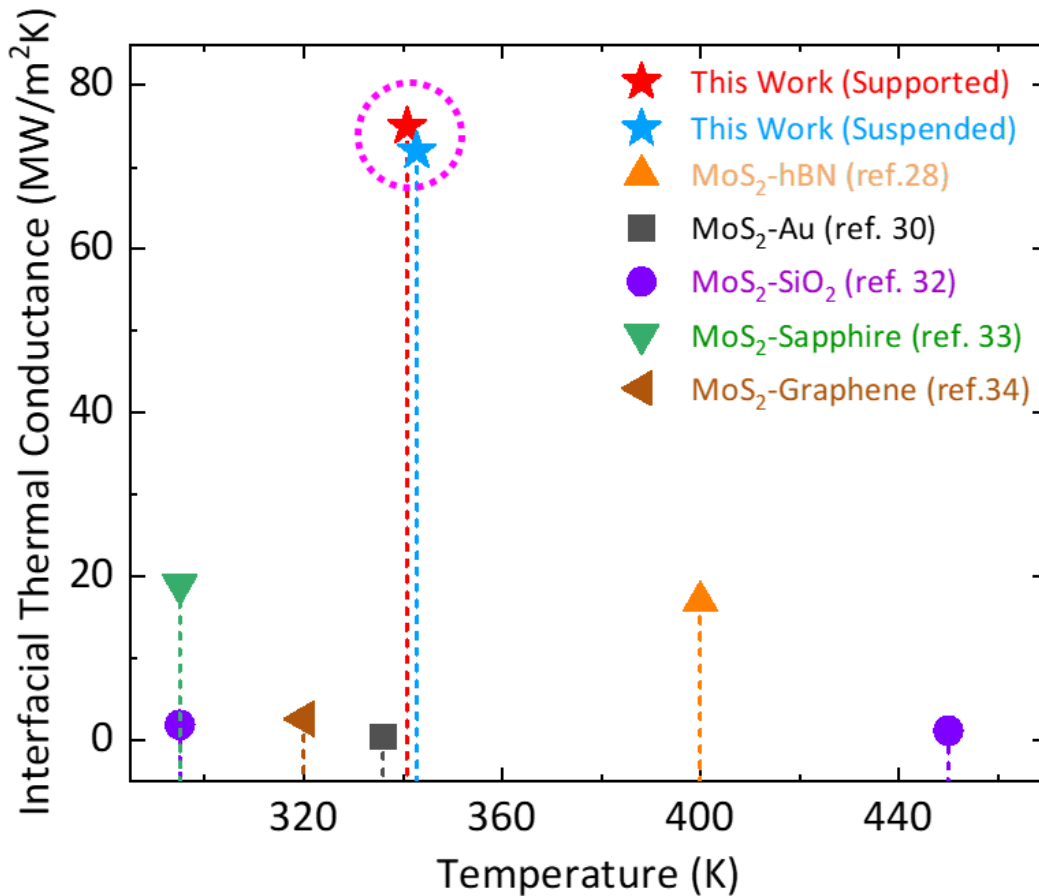


Figure 5. Benchmark of heat thermal management in hBN/MoS₂/hBN van der Waals heterostructure in this work. Comparison of interfacial thermal conductance in hBN encapsulated MoS₂ and other device structures.

Conclusions

In conclusion, we have reported the first discovery of the thermal transport properties of hBN encapsulated MoS₂ van der Waals heterostructure, and revealed the very high interfacial thermal conductance between hBN and MoS₂. By studying Raman spectroscopy under different temperatures and applied laser power, lateral thermal conductivity of hBN and MoS₂ and interfacial thermal conductance between different interfaces are discovered. In particular, we found that the interfacial thermal conductance in hBN/MoS₂/hBN encapsulated structure is 72 ± 22 MW/m²K in the supported area and 74 ± 25 MW/m²K in the suspended area, which are significantly higher than other structures. The estimated interfacial thermal conductance is consistent with theoretical analysis using MD simulation. These results demonstrate that the hBN encapsulated structure provides efficient heat dissipation pathways for encapsulated 2D material and paves way for building high-performance hBN encapsulated 2D materials nanoelectronics.

Methods

Suspended hBN/MoS₂/hBN van der Waals Heterostructure Device Fabrication

The fabrication of hBN/MoS₂/hBN van der Waals heterostructure device starts from exfoliating hBN and MoS₂ on PDMS. After selecting ideal hBN and MoS₂, bottom hBN, MoS₂, top hBN are transferred onto pre-patterned substrates with micro trenches using an all-dry transfer method with careful alignments under microscope [37].

Raman Scattering and Photoluminescence Measurement

The hBN/MoS₂/hBN heterostructure device is measured using a RENISHAW InVia Raman Microscope system with a 514 nm laser. In the temperature dependent Raman measurement, heterostructure samples are heated uniformly from 295K to 495K using a heating stage (Linkam Stage THMS600). The laser power is kept below 100 μ W during the measurement to reduce additional laser heating. In both temperature dependent measurement and power dependent measurement, the laser is focused on supported and suspended regions.

Atomic Force Microscopy (AFM) Measurement

Atomic force microscope (AFM) (Bruker Dimension Icon) is used to measure the thickness of top and bottom hBN layers. The AFM tapping mode in air is used.

Acknowledgement: We thank the financial support from Stevens Institute of Technology's startup funding, Stevens Institute of Technology's Bridging Award, and Brookhaven National Laboratory Center for Functional Nanomaterials. The work at Case Western Reserve University is supported by National Science Foundation CAREER Award (Grant ECCS-1454570) and CCSS Award (Grant ECCS-1509721).

Corresponding Author

*Baoping Xu. Email: bx4c@virginia.edu

*Philip Feng. Email: philip.feng@ufl.edu

*Xian Zhang. Email: xzhang4@stevens.edu

Reference

- 1 Novoselov, K. S. *et al.* Electric field effect in atomically thin carbon films. *Science* **306**, 666–669 (2004).
- 2 Radisavljevic, B., Radenovic, A., Brivio, J., Giacometti, V. & Kis, A. Single-layer MoS₂ transistors. *Nat. Nanotechnol.* **6**, 147–150 (2011).
- 3 Dean, C. R. *et al.* Boron nitride substrates for high-quality graphene electronics. *Nat. Nanotechnol.* **5**, 722–726 (2010)
- 4 Mak, K. F., Lee, C., Hone, J., Shan, J. & Heinz, T. F. Atomically Thin MoS₂: A new direct-gap semiconductor. *Phys. Rev. Lett.* **105**, 136805 (2010).
- 5 Novoselov, K. S. *et al.* Two-dimensional gas of massless Dirac fermions in graphene. *Nature* **438**, 197–200 (2005).
- 6 Geim, A. K. & Grigorieva, I. V. Van der Waals heterostructures. *Nature* **499**, 419 (2013).
- 7 Wang, Q. H., Kalantar-Zadeh, K., Kis, A., Coleman, J. N. & Strano, M. S. Electronics and optoelectronics of two-dimensional transition metal dichalcogenides. *Nat. Nanotechnol.* **7**, 699–712 (2012).
- 8 Cui, X. *et al.* Multi-terminal transport measurements of MoS₂ using a van der Waals heterostructure device platform. *Nat. Nanotechnol.* **10**, 534–540 (2015).
- 9 Britnell, L. *et al.* Strong Light-Matter Interactions in Heterostructures of Atomically Thin Films. *Science* **340**, 1311–1314 (2013).
- 10 Li, Y. *et al.* Measurement of the optical dielectric function of monolayer transition-metal dichalcogenides: MoS₂, MoSe₂, WS₂, and WSe₂. *Phys. Rev. B* **90**, 205422 (2014).
- 11 Yuan, H. *et al.* Generation and electric control of spin–valley-coupled circular photogalvanic current in WSe₂. *Nat. Nanotechnol.* **9**, 851–857 (2014).
- 12 Lee, C., Wei, X., Kysar, J. W. & Hone, J. Measurement of the elastic properties and intrinsic strength of monolayer graphene. *Science* **321**, 385–8 (2008).
- 13 Wu, W. *et al.* Piezoelectricity of single-atomic-layer MoS₂ for energy conversion and piezotronics. *Nature* **514**, 470–474 (2014).
- 14 Wu, S. *et al.* Multiple hot-carrier collection in photo-excited graphene Moiré superlattices. *Sci. Adv.* **2**, e1600002 (2016).
- 15 Xia, F., Mueller, T., Lin, Y., Valdes-Garcia, A. & Avouris, P. Ultrafast graphene photodetector. *Nat. Nanotechnol.* **4**, 839–843 (2009).
- 16 Bunch, J. S. *et al.* Electromechanical resonators from graphene sheets. *Science* **315**, 490–493 (2007).
- 17 Kim, Y. D. *et al.* Bright visible light emission from graphene. *Nat. Nanotechnol.* **10**, 676–681 (2015).
- 18 Wang, L. *et al.* One-dimensional electrical contact to a two-dimensional material. *Science* **342**, 614–617 (2013).

-
- 19 Tongay, S. *et al.* Tuning interlayer coupling in large-area heterostructures with CVD-grown MoS₂ and WS₂ monolayers. *Nano Lett.* **14**, 3185–3190 (2014).
 - 20 Li, Y. *et al.* Gate-Tuned temperature in a hexagonal boron nitride-encapsulated 2-D semiconductor device. *IEEE Trans. Electron Devices* **65**, 4068–4072 (2018).
 - 21 Gao, Y. *et al.* High-speed electro-optic modulator integrated with graphene-boron nitride heterostructure and photonic crystal nanocavity. *Nano Lett.* **15**, 2001–2005 (2015).
 - 22 Lee, G.-H. *et al.* Highly stable, dual-gated MoS₂ transistors encapsulated by hexagonal boron nitride with gate-controllable contact, resistance, and threshold voltage. *ACS Nano* **9**, 7019–7026 (2015).
 - 23 Yuan, C. *et al.* Modulating the thermal conductivity in hexagonal boron nitride via controlled boron isotope concentration. *Commun. Phys.* **2**, 43 (2019).
 - 24 Gong, Y. *et al.* Thermal conductivity and Seebeck coefficients of icosahedral boron arsenide films on silicon carbide. *J. Appl. Phys.* **108**, 84906 (2010).
 - 25 Cai, Q. *et al.* High thermal conductivity of high-quality monolayer boron nitride and its thermal expansion. *Sci. Adv.* **5**, eaav0129 (2019).
 - 26 Jo, I. *et al.* Thermal Conductivity and Phonon Transport in Suspended Few-Layer Hexagonal Boron Nitride. *Nano Lett.* **13**, 550–554 (2013).
 - 27 Zhou, H. *et al.* High thermal conductivity of suspended few-layer hexagonal boron nitride sheets. *Nano Res.* **7**, 1232–1240 (2014).
 - 28 Liu, Y. *et al.* Thermal conductance of the 2D MoS₂/BN and graphene/BN interfaces. *Sci. Rep.* **7**, 43886 (2017).
 - 29 Yalon, E. *et al.* Energy dissipation in monolayer mos₂ electronics. *Nano Lett.* **17**, 3429–3433 (2017).
 - 30 Zhang, X. *et al.* Measurement of lateral and interfacial thermal conductivity of single- and bilayer MoS₂ and MoSe₂ using refined optothermal Raman technique. *ACS Appl. Mater. Interfaces* **7**, 25923–25929 (2015).
 - 31 Yan, R. *et al.* Thermal conductivity of monolayer molybdenum disulfide obtained from temperature-dependent Raman spectroscopy. *ACS Nano* **8**, 986–993 (2014).
 - 32 Taube, A., Judek, J., Łapińska, A. & Zdrojek, M. Temperature-dependent thermal properties of supported MoS₂ monolayers. *ACS Appl. Mater. Interfaces* **7**, 5061–5065 (2015).
 - 33 Yasaei, P. *et al.* Interfacial thermal transport in monolayer MoS₂- and graphene-based devices. *Adv. Mater. Interfaces* **4**, 1700334 (2017).
 - 34 Yue, X. F. *et al.* Measurement of interfacial thermal conductance of few-layer MoS₂ supported on different substrates using Raman spectroscopy. *J. Appl. Phys.* **127**, 104301 (2020).
 - 35 Yang, R., Zheng, X., Wang, Z., Miller, C. J. & Feng, P. X.-L. Multilayer MoS₂ transistors enabled by a facile dry-transfer technique and thermal annealing. *J. Vac. Sci. Technol. B* **32**, 61203 (2014).
 - 36 Balandin, A. A. *et al.* Superior thermal conductivity of single-layer graphene. *Nano Lett.* **8**, 902–907 (2008).

-
- 37 Jin-Xiang, D. *et al.* Optical properties of hexagonal boron nitride thin films deposited by radio frequency bias magnetron sputtering. *Chinese Phys. B* **18**, 4013–4018 (2009).
- 38 Cai, W. *et al.* Thermal Transport in Suspended and Supported Monolayer Graphene Grown by Chemical Vapor Deposition. *Nano Lett.* **10**, 1645–1651 (2010).
- 39 Li, X. *et al.* Thermal conduction across a boron nitride and SiO₂ interface. *J. Phys. D. Appl. Phys.* **50**, 104002 (2017).
- 40 Han, X., Lin, J., Liu, J., Wang, N. & Pan, D. Effects of hexagonal boron nitride encapsulation on the electronic structure of few-layer MoS₂. *J. Phys. Chem. C* **123**, 14797–14802 (2019).
- 41 Los, J. H. *et al.* Extended tersoff potential for boron nitride: energetics and elastic properties of pristine and defective h-BN. *Phys. Rev. B* **96**, 184108 (2017).
- 42 Jiang, J.-W., Park, H. S. & Rabczuk, T. Molecular dynamics simulations of single-layer molybdenum disulphide (MoS₂): Stillinger-Weber parametrization, mechanical properties, and thermal conductivity. *J. Appl. Phys.* **114**, 64307 (2013).
- 43 Justo, J. F., Bazant, M. Z., Kaxiras, E., Bulatov, V. V & Yip, S. Interatomic potential for silicon defects and disordered phases. *Phys. Rev. B* **58**, 2539–2550 (1998).
- 44 Yuan, P., Li, C., Xu, S., Liu, J. & Wang, X. Interfacial thermal conductance between few to tens of layered-MoS₂ and c-Si: Effect of MoS₂ thickness. *Acta Mater.* **122**, 152–165 (2017).
- 45 Farahani, H., Rajabpour, A., Khanaki, M. & Reyhani, A. Interfacial thermal resistance between few-layer MoS₂ and silica substrates: a molecular dynamics study. *Comput. Mater. Sci.* **142**, 1–6 (2018).
- 46 Okada, M. *et al.* Direct Chemical Vapor Deposition Growth of WS₂ Atomic Layers on Hexagonal Boron Nitride. *ACS Nano* **8**, 8273–8277 (2014).